Structural Engineering and Mechanics, *Vol. 74, No. 1 (2020) 19-32*
DOI: https://doi.org/10.12989/sem.2020.74.1.019

Influence of neck width on the performance of ADAS device with diamond-shaped hole plates

Yingxiong Wu[1a], Jianfeng Lu[2b] and Yun Chen*[3]

[1]*College of Civil Engineering, Fuzhou University, No.2 North Avenue of Wulong River, Fuzhou, Fujian, China*
[2]*Department of Civil and Environmental Engineering, Harbin Institute of Technology (Shenzhen), Taoyuan Street, Nanshan District, Shenzhen, Guangdong, China*
[3]*Nantong LANKE Damping Technology Co., Ltd. No.1101 Xinkai Street, Chongchuan District, Nantong, Jiangsu, China*

(Received June 12, 2019, Revised August 1, 2019, Accepted November 12, 2019)

Abstract. Metallic energy-dissipation dampers are widely used in structures. They are comprised of an added damping and stiffness (ADAS) device with many parallel, diamond-shaped hole plates, the neck width of which is an important parameter. However, no studies have analyzed the neck width's influence on the ADAS device's performance. This study aims to better understand that influence by conducting a pseudo-static test on ADAS, with three different neck widths, and performing finite element analysis (FEA) models. Based on the FEA results and mechanical theory, a design neck width range was proposed. The results showed that when the neck width was within the specified range, the diamond-shaped hole plate achieved an ideal yield state with minimal stress concentration, where the ADAS had an optimal energy dissipation performance and the brittle shear fracture on the neck was avoided. The theoretical values of the ADAS yield loads were in good agreement with the test values. While the theoretical value of the elastic stiffness was lower than the test value, the discrepancy could be reduced with the proposed modified coefficient.

Keywords: ADAS device; diamond-shaped hole plates; neck width; pseudo-static test; metallic energy-dissipation dampers

1. Introduction

Metallic energy-dissipation dampers are widely used in structures due to their simple configuration and stable performance (Wang 2017). They use plastic deformation caused by shearing or bending metal materials to dissipate seismic energy; e.g., a shear energy dissipation damper and a bending energy dissipation damper (Skinner *et al*. 2010). Moreover, their geometry has a significant impact on their performance (Mirzaei *et al*. 2012).

A shear energy dissipation damper is a rectangular plate (the initial shape) designed to produce a plastic strengthening effect (Nakashima 1995). A rectangular strip is formed by slotting rectangular seams on the shear plate (Ke and Chen 2014), allowing the damper to dissipate energy before the structural member is damaged (Chan and Albermani 2008). A strip with a defined slenderness ratio can also prevent the damper from buckling (Hedayat and Ahmad 2015) . The strip shape is optimized into either a variable section dumbbell strip, a tapered strip, or an hourglass strip. This type of damper has a uniform strain and improves energy dissipation and fatigue performance, especially in the parabolic hourglass strip configuration (Ghabraie *et al*. 2010, Xu *et al*. 2010, Teruna *et al*. 2015, Lee *et al*. 2015, Deng *et al*. 2014).

The bending energy dissipation damper can be a triangle (Tsai *et al*. 1993), an X shape (Whittaker *et al*. 1991), a diamond shape (Shih and Sung 2005), a diamond-shaped hole (Xing and Guo 2003), or an hourglass shape (Llera *et al*. 2010), all having unique, but uniform, strain characteristics. To make the dissipation capacity of the metallic energy damper similar in two directions, Basu *et al*. (2016) designed a solid hourglass damper. Then, Briones *et al*. (2014) hollowed out the solid hourglass damper, which increased the dissipation capacity and reduced material cost. Traditional energy dissipation components are mounted on herringbone braces or walls (Vosooq and Zahrai 2013, Zhang *et al*. 2015). In recent years, these components, such as X-shaped steel plates (Sabouri and Payandehjoo 2017) and round steel bars (Aghlara and Tahir 2018), have been embedded into inclined braces, thereby reducing damage to the main structure. For this study, a diamond-shaped hole plate (DH plate) is embedded into the brace to form a braced damper, as shown in Fig. 1. The DH plate uses plastic deformation resulting from bending metal materials to dissipate seismic energy.

The narrowest part of the DH plate is called the neck, as shown in Fig. 1. Under load, strain energy is concentrated in the damper neck. If the height to thickness ratio of the hourglass out-of-plane bending energy dissipation damper is increased, the strain concentration in the neck would also increase (Llera *et al*. 2010). With a solid hourglass damper, the neck width has little influence on its dissipation capacity

*Corresponding author, M.Sc.
E-mail: m18060849026@163.com
[a] Associate Professor
E-mail: wyxfz2006@163.com
[b] Ph.D. Student
E-mail: lujianfengfd@foxmail.com

http://www.techno-press.com/journals/sem&subpage=7
ISSN: 1225-4568 (Print), 1598-6217 (Online)

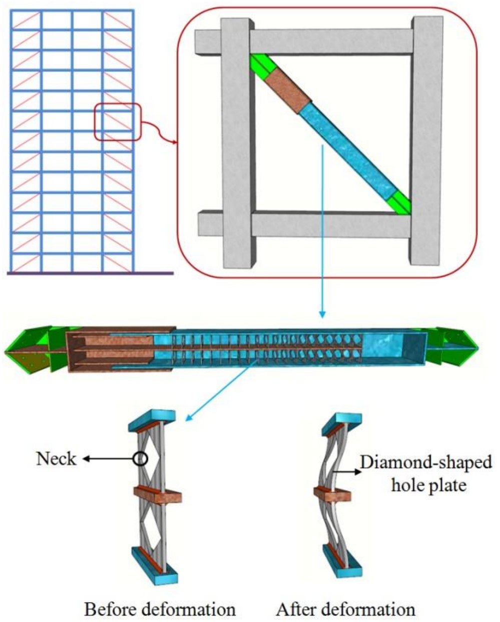

Fig. 1 ADAS device with DH plate (braced damper)

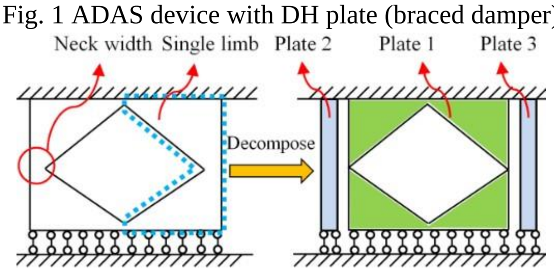

Fig. 2 Decomposition diagram of the DH plate

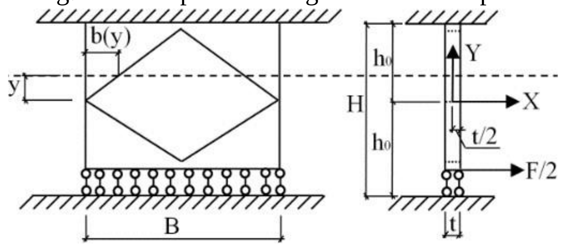

Fig. 3 Plate 1 coordinate system

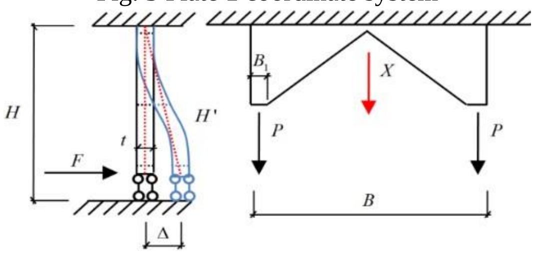

Fig. 4 Neck film effect

(Basu and Reddy 2016). Parabolic slit dampers could alleviate the strain concentration by increasing the neck width (Xu *et al*. 2010). Therefore, the neck width significantly influences the out-of-plane bending energy dissipation damper's performance. Hence, the DH plate's neck width is an important design parameter of an added damping and stiffness (ADAS) device. However, no studies have analyzed the neck width's influence on the ADAS device's performance.

Chan *et al*. (2008) introduced the modified coefficient in the theoretical equation for calculating the steel damper's elastic stiffness after considering the influence of the damper boundary condition. This coefficient was determined from test results (Xu *et al*. 2010, Lee *et al*. 2015, Lee *et al*. 2016) and ranged from 0.3 to 0.8. Unfortunately, the coefficient is only applicable to dampers with a specific size and configuration. Thus, it is necessary to systematically analyze the modified coefficient parameters for a variety of damper configurations.

To study the neck width's influence on the DH plate damping system performance, a theoretical equation for the ADAS performance parameters was derived that takes the neck width into consideration. Next, quasi-static tests were carried out on ADAS models with different neck widths. Then, finite element analysis (FEA) models were created to simulate the ADAS test models, and the FEA model's accuracy was verified by the test results. Finally, based on the FEA results and mechanic theory, a design neck width range and a modified elastic stiffness equation were proposed. Our results could provide a reference for the theoretical design of ADAS parameters.

2. Theoretical analysis

2.1 Performance parameters

To simplify the calculation, the DH plate was decomposed into three parts. As shown in Fig. 2, the conventional theoretical calculation only considers Plate 1, ignoring Plates 2 and 3's influence on performance parameters. The neck can transmit the axial force and shear force in the DH plate. To consider the influence of the neck width on the damper's performance, the performance parameters of the three parts are calculated below.

(1) Performance parameters of Plate 1

The coordinate system for Plate 1 is shown in Fig. 3.

Because the DH plate's deformation is anti-symmetric along the X-axis, force analysis was carried out on the positive part of the Y-axis. The plate section stress, σ_1, at a point on the plate is

$$\sigma_1 = \frac{M_1(y)x}{I_{Z1}(y)} \tag{1}$$

where $M_1(y)$ is the bending moment of the section at height y, x is the distance from the neutral axis of the section to the point in the thickness direction, and

$$M_1(y) = \frac{2yM_B}{H}, \quad I_{Z1}(y) = \frac{2b(y)t^3}{12} = \frac{Bt^3}{6H}y$$

where M_B is the bending moment at the upper end of Plate 1. Hence, the stress at a point on the plate can be written as

$$\sigma_1 = \frac{12M_Bx}{Bt^3} \tag{2}$$

As shown in Eq. (2), for a specific DH plate at a specific moment, the only variable in the section stress σ_1 is x, indicating that the stress at each point of the same thickness along the y-direction is equal, and that Plate 1 can achieve the ideal energy dissipation state of simultaneous yield at each point along the y-axis.

When the edge of the plate yields, the DH plate enters the yield state, and the cross-section reaches the yield bending moment. At this time, $\sigma_1 = f_y$, $x = t/2$, where f_y is the yield stress of the plate and the bending moment of the plate $M_{1y}(y)$ is

$$M_{1y}(y) = \frac{f_y B t^2}{3H} y \tag{3}$$

The yield shear force of Plate 1, F_{1Q}, is

$$F_{1Q} = F_{1Q}(y) = \frac{M_{1y}(y)}{y} = \frac{f_y t^2 B}{3H} \tag{4}$$

When the plate yields, the bending moment of the section at height y along the DH plate is $M'_{1y}(y)$ and the shear force $F'_{1Q}(y)$ is

$$M'_{1y}(y) = \frac{M_{1y}(H/2)}{H/2} y = \frac{f_y B t^2}{3H} y = M_{1y}(y) \tag{5}$$

$$F'_{1Q}(y) = F_{1Q} = \frac{f_y t^2 B}{3H} \tag{6}$$

When a unit load is applied to the x-direction at the bottom of the DH plate, $\overline{M'_{1y}(y)}$ and $\overline{F'_{1Q}(y)}$ are respectively the bending moment and shear force of the section at height y given by:

$$\overline{M'_{1y}(y)} = \frac{2}{H}\frac{H}{2} y = y \tag{7}$$

$$\overline{F'_{1Q}(y)} = 1 \tag{8}$$

When the DH plate yields, the axis curvature k and the shear modulus G are:

$$k_1 = \frac{1}{\rho_1} = \frac{M'_{1y}(y)}{EI_{Z1}(y)} = \frac{2 f_y}{Et} \tag{9}$$

$$G = \frac{E}{2(1+\nu)} \tag{10}$$

where $\nu = 0.3$ is the Poisson's ratio and E is the material's elastic modulus. At height y, the area $A_1(y)$, enclosed by the neutral axis of the section to the edge of the DH plate, is

$$A_1(y) = 2b(y)\frac{t}{2} = 2\frac{By}{H}\frac{t}{2} = \frac{Bt}{H} y \tag{11}$$

According to the principle of virtual work, the displacement δ_1 at the top of the steel plate relative to the middle height in the yield state is

$$\begin{aligned}1\times\delta_1 &= \int_0^{H/2} \frac{M'_{1y}(y)\overline{M'_{1y}(y)}}{EI_{Z1}(y)} dy + \int_0^{H/2} \frac{kF'_{1Q}(y)\overline{F'_{1Q}(y)}}{GA_1(y)} dy \\ &= \frac{1}{E}\int_0^{H/2} \frac{f_y B t^2 y^2}{3H}\frac{6H}{Bt^3 y} dy + \int_1^{H/2} \frac{2 f_y}{Et}\frac{f_y t^2 B}{3H}\frac{2(1+\nu)}{E}\frac{H}{Bty} dy \\ &= \frac{1}{E}\int_0^{H/2} \frac{2 f_y y}{t} dy + \int_1^{H/2} \frac{4 f_y^2 (1+\nu)}{3E^2 y} dy \\ &= \frac{f_y H^2}{4Et} + \frac{4 f_y^2 (1+\nu)}{3E^2} \ln\frac{H}{2}\end{aligned}$$

When $H/t > 10$, the second term in the equation above is much smaller than the first term, so it can be omitted. Therefore, the yield displacement and the elastic stiffness of Plate 1 are:

$$\Delta_{y1} = 2\delta_1 = \frac{f_y H^2}{2Et} \tag{12}$$

$$K_1 = \frac{F_{1Q}}{\Delta_{y1}} = \frac{f_y t^2 B}{3H}\frac{2Et}{f_y H^2} = \frac{2EBt^3}{3H^3} \tag{13}$$

(2) Performance parameters of Plate 2

According to Section 2.1(1), $b(y) = B_1$, where B_1 is the neck width of the DH plate. Similar to the above calculation, Plate 2's performance parameters can be calculated, including the yield shear force, yield displacement, and elastic stiffness, as follows:

$$F_{2Q} = \frac{f_y B_1 t^2}{3H} \tag{14}$$

$$\Delta_{y2} = \frac{f_y H^2}{3Et} \tag{15}$$

$$K_2 = \frac{EB_1 t^3}{H^3} \tag{16}$$

(3) Damper's performance parameters

Because Plates 2 and 3 have the same mechanical behavior, the yield shear, elastic stiffness, and yield displacement of ADAS with n DH plates are:

$$F_Q = nF_{4Q} = \frac{2nf_y t^2 (B + 2B_1)}{3H} \tag{17}$$

$$K = nK_4 = \frac{2nEt^3 (2B + 6B_1)}{3H^3} \tag{18}$$

$$\Delta_y = \frac{F_Q}{K} = \frac{f_y H^2}{Et}\frac{(B + 2B_1)}{(2B + 6B_1)} \tag{19}$$

The three equations above show that, as the neck width B_1 increases, the elastic stiffness and the yield load increase while the yield displacement decreases slightly. Therefore, it is recommended that the neck width's influence on the damper's performance parameters should not be neglected in the damper design.

2.2 Minimum neck width

The minimum neck width has little influence on the yield shear force, so the ultimate shear of the DH plate F_p is 1.5 times the yield shear of Plate 1 given by:

$$F_p = \frac{3}{2} F_{1Q} = \frac{f_y t^2 B}{2H} \tag{20}$$

$\tau_{\max}$ is the peak shear stress of the neck section when the DH plate bends given by:

$$\tau_{\max} = \frac{3}{2}\frac{F_p}{A} = \frac{3}{2}\frac{1}{2B_1 t}\frac{f_y t^2 B}{2H} = \frac{3 f_y tB}{8B_1 H} \tag{21}$$

The yield shear strength is $f_{vy} = \frac{f_y}{\sqrt{3}}$. To avoid shear failure in the plate, the neck section stress should satisfy $\tau_{\max} \le f_{vy}$, so the neck width B_1 should meet:

$$B_1 \ge \frac{3\sqrt{3}Bt}{8H} \tag{22}$$

Hence, the minimum neck width B_{min} is

$$B_{\min} = \frac{3\sqrt{3}Bt}{8H} \tag{23}$$

When the damper is theoretically designed, the neck width should be greater than the minimum neck width B_{min}, ensuring that, under the ultimate shear force, the neck does not suffer from shear failure before the other parts.

2.3 Neck film effect

When the DH plate's lateral displacement along the thickness direction is Δ, the plate length increases from H to H', as shown in Fig. 4. The height change Δ_H of the plate during the lateral movement is

$$\Delta_H = \sqrt{H^2 + \Delta^2} - H \approx \frac{\Delta^2}{2H} \tag{24}$$

The height change could cause film strain, which produces film stress and film internal force P in the neck section. ADAS is a displacement damper with boundary conditions, constraining Δ_H. Thus, the influence of film strain in the neck section on the damper's performance should be considered. When the neck width B_1 is rather small, the film strain is significant.

3. Test analysis

3.1 DH plate size

In the pseudo-static test, the structure height h was 3 m. According to the DH plate fatigue test equation (Xing and Guo 2003), $\frac{H^2}{t} \ge 0.873h$, where the height, thickness, and width of the DH plate can be determined as H = 150 mm, t = 8 mm, and B = 280 mm, respectively. Eq. (23) was used to determine the minimum neck width B_{min} as

$$B_{\min} = \frac{3\sqrt{3}Bt}{8H} = \frac{3\sqrt{3}\times 280\times 8}{8\times 150} = 9.70mm$$

To distinguish the influence of different neck widths on ADAS performance, three neck widths were selected; i.e., 5, 10, and 35 mm. The samples with these three neck widths were named as HNQ-5, HNQ-10, and HNQ-35, respectively, where the neck width of HNQ-10 was assumed to be the design neck width.

To alleviate the sudden change of the section in the neck region, we adopted a circular fillet for the neck. Taking B_1 = 35 mm as an example, the determination of the fillet radius, R, is shown in Fig. 5 and was obtained by the equation:

$$R = \frac{HB_1}{\sqrt{B^2 + H^2} - H} \tag{25}$$

3.2 Test model and loading device

The ADAS test model's simplified design is shown in Fig. 6. The cushion block was temporary and was removed before the test. Fifty percent of the welds were tested for flaw detection, and they conformed to the grade II weld requirements of the Chinese code. The test model was loaded by an MTS244.31 250kN actuator, as shown in Fig. 7. The top plate and the actuator were connected via a bolt, and the horizontal plate and the base were connected via the bolt. The actuator provided a cyclic vertical load. The DH plate was subjected to out-of-plane deformation by the core plate to simulate the reciprocating action of the damper during an earthquake.

3.3 Loading system and data collection

(1) Loading system

The loading system was comprised of variable-amplitude loading and constant-amplitude loading. The sequence of variable-amplitude loading is illustrated in Fig. 8. The ADAS was first loaded at an amplitude of 2 mm (< yield displacement) for three cycles, and then at an amplitude of 3 mm (≈ yield displacement) for three cycles, and finally at each amplitude for three cycles. The force was increased until cracks appeared in the welds. The constant-amplitude loading was cyclic, with a constant displacement amplitude of 18 mm, which was maintained until the DH plate fractured. The loading rate was held constant at 0.5 mm/s.

(2) Data collection

The restoring force and damper displacement were read by the MTS loading system. Two YHD-200 displacement meters were arranged diagonally on the damper's top plate to verify the displacement. The DH plate strain was recorded by a DH3816 acquisition system with six uniaxial strain gauges pasted on each surface of the two top plates on the damper test model. The number and arrangement of the strain gauges are shown in Fig. 9.

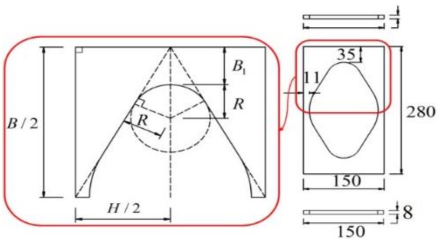

Fig. 5 Fillet radius and plate dimensions

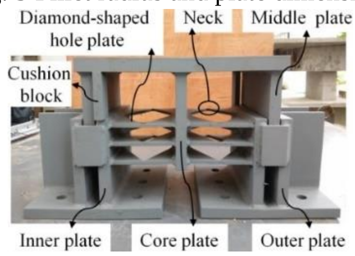

Fig. 6 The test model

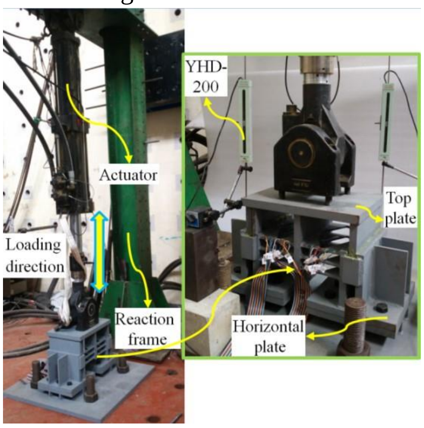

Fig. 7 Loading device

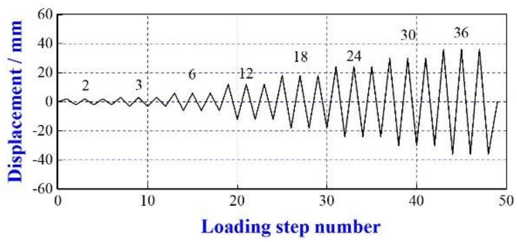

Fig. 8 Variable-amplitude loading system

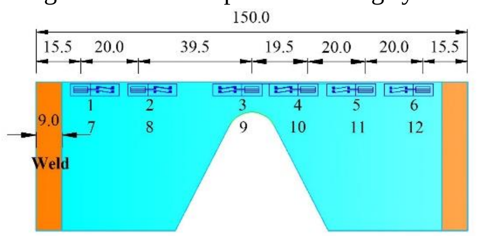

(a) Lower surface of the DH plate

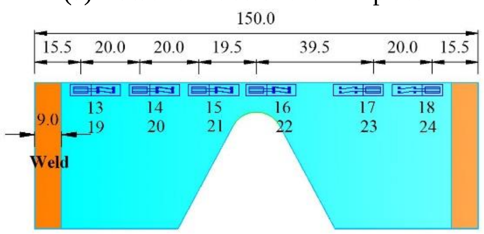

(b) Upper surface of the DH plate

Fig. 9 Strain gauge number and arrangement

3.4 Test discussion and failure modes

(1) Variable-amplitude loading

HNQ-5

No cracks were visible in the welds or the neck until the displacement reached 36 mm, where the neck abruptly sheared through with signs of brittle fracture, as shown in Fig. 10. The displacement energy was concentrated in the neck, indicating poor energy dissipation performance.

HNQ-10

By the time the variable displacement reached 36 mm, there were five cracks near the fillet, with lengths varying from 5 to 20 mm and approximately 0.3-mm wide and 0.3-mm deep.

HNQ-35

At a displacement of 36 mm, there were 12 cracks near the fillet, with lengths varying from 10 to 35 mm and approximately 0.5-mm wide and 0.5-mm deep. The bending deformation and energy dissipation were concentrated in the area around the welds and not the neck.

(2) Constant-amplitude loading

The failure modes under constant amplitude cyclic loading are shown in Fig. 11.

HNQ-10

After 60 cycles, there was one crack through the fillet weld in the direction of the DH plate thickness and several cracks through the DH plate at the neck. After 86 cycles, the neck failed. As can be seen in Fig. 11, the fracture surface was rough, signifying low cycle fatigue failure. The ratio of the number of surface cracks near the inner plate to the number of surface cracks near the core plate was 5:3.

The cracks appeared in the fillet; then the fillet and neck before fatigue fracture occurred in the neck. These low cycle fatigue cracks were distributed through the weldment, signifying an even and efficient dissipation of energy.

HNQ-35

After 60 cycles, there were three cracks through the fillet weld in the direction of the thickness. After 152 cycles, cracks developed in the inner side of the single limb, and a full-length fracture appeared near the core plate fillet. The fracture section was rough, signifying low cycle fatigue fracture. The unpenetrated cracks were near the inner plate, and the DH plate neck had no cracks.

HNQ-35 initially had cracks in the fillet toe, then developed cracks along the fillet, and finally, a full-length fracture appeared through the base metal at the toe of the fillet. However, there was no fatigue fracture in the neck. The failure only occurred at the fillet; hence, the energy dissipation performance was poorly distributed. Most of the cracks were in the fillet on one side of the core plate, indicating that the fillet of the core plate was more prone to crack damage.

3.5 Test data analysis

3.5.1 Material performance test

The specimen size of the DH plate material (Q235B) is shown in Fig. 12(a). The tested stress-strain curves of the material are shown in Fig. 12(b).

The average yield strength of the three specimens was 306.33 MPa, the average ultimate strength was 512.43 MPa,

(a) Front view

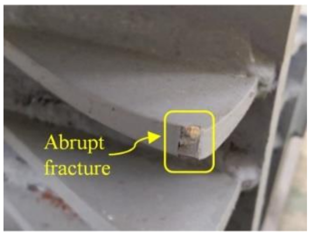

(b) Section

Fig. 10 HNQ-5 failure mode

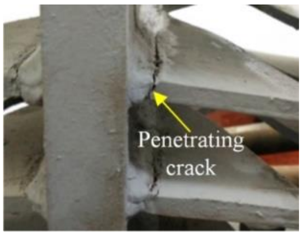

(a) HNQ-10 fillet crack (60 cycles)

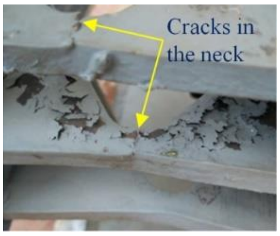

(b) HNQ-10 neck crack (60 cycles)

(c) HNQ-10 neck fracture (86 cycles)

(d) HNQ-10 fracture section

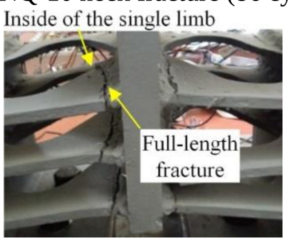

(e) HNQ-35 fillet crack (152 cycles)

(f) HNQ-35 fracture section (152 cycles)

Fig. 11 Failure modes under constant-amplitude loading

the average elastic modulus was 210 GPa, and the average elongation at break was 25.98%.

3.5.2 Hysteresis loop

The variable-amplitude hysteresis loops of the ADAS test models are shown in Fig. 13.

When the displacement was less than 3 mm, the hysteresis loop was almost straight, indicating that the damper remained in the elastic state. When the displacement exceeded 3 mm, the hysteresis loop began to bend toward the X-axis, indicating that the damper remained in the inelastic state. After the neck abruptly sheared through, HNQ-5's bearing capacity was reduced to half the original under reverse loading in the first cycle; hence, the neck width should not be too small in order to avoid early damper failure in large earthquakes. The hysteresis loop with a displacement less than 24 mm presented a more apparent fusiform shape, and the hysteresis loop was fuller, indicating improved energy absorption. The hysteresis loop with a displacement greater than 24 mm began to exhibit the pinch effect, indicating

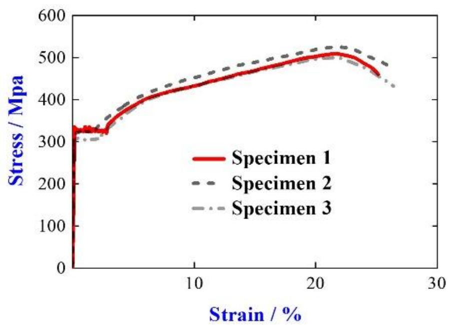

(a) Specimen size

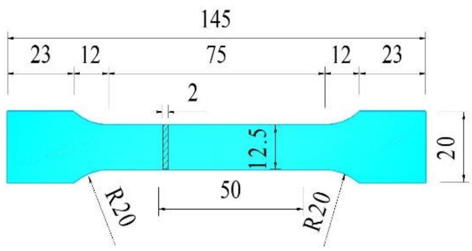

(b) Stress-strain curves

Fig. 12 Specimen size and stress-strain curves

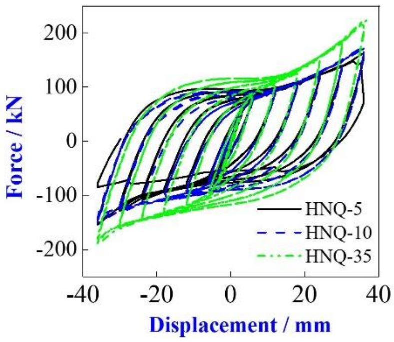

Fig. 13 Hysteresis loops

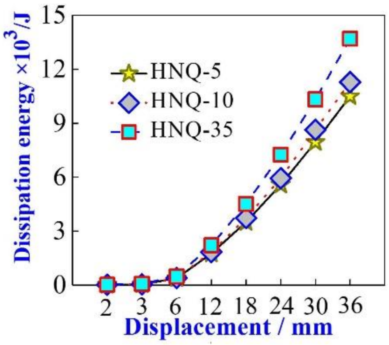

Fig. 14 Dissipation energy

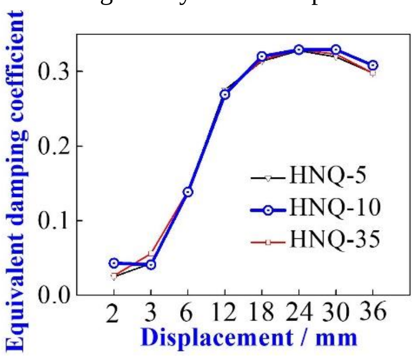

Fig. 15 Equivalent damping coefficient

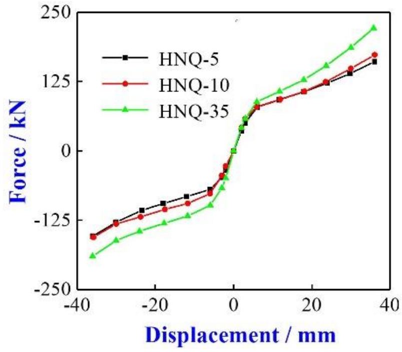

Fig. 16 Skeleton curves

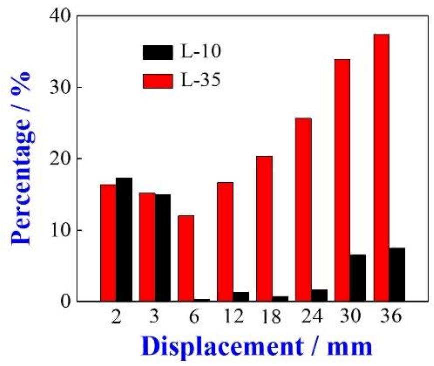

Fig. 17 Percentage difference in the bearing capacity vs HNQ-5

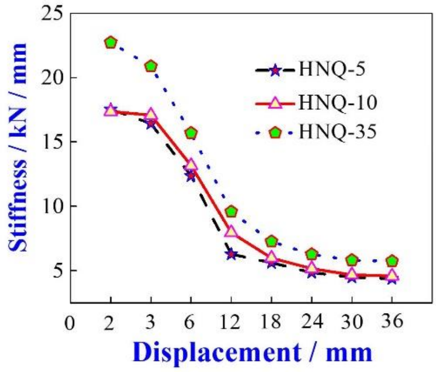

Fig. 18 Equivalent secant stiffness

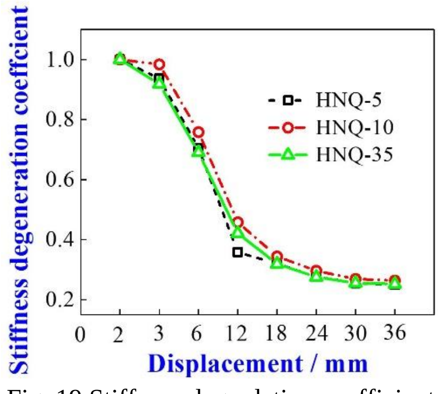

Fig. 19 Stiffness degradation coefficient

energy dissipation instability in the damper. This is because the DH plate absorbs a tensile force along its height at a large displacement. The pinch effect of HNQ-35 was more obvious than that of HNQ-5, indicating that reducing the neck width improved the damper's pinch effect. HNQ-10's hysteresis performance was the most stable.

3.5.3 Energy dissipation performance

The ADAS test models' dissipation energy and equivalent damping coefficient are shown in Fig 14 and Fig. 15, respectively.

(1) As the neck width increased, the damper's dissipation energy significantly increased. As the

displacement increased past 12 mm, the increase in displacement-dissipation energy became linear. Moreover, the dissipation energy growth rate also increased with the neck width, indicating that increasing the neck width increases the damper's dissipation energy.

(2) After the damper began to dissipate energy, the equivalent damping coefficient of the three dampers was almost identical, and the equivalent damping coefficient grew rapidly; this behavior was conducive to achieving earlier energy dissipation potential. When the displacement was greater than 24 mm, HNQ-10's equivalent damping coefficient was greater than those of HNQ-5 and HNQ-35. Therefore, HNQ-10's energy dissipation capacity was greater than those of HNQ-5 and HNQ-35. In addition, HNQ-10 remained stable for a long period near the optimal equivalent damping coefficient and entered the falling section later in the equivalent damping coefficient, so its energy dissipation stability was greater than those of HNQ-5 and HNQ-35.

(3) The optimal equivalent damping coefficient of the hourglass shape damper close to the test conditions was 0.268 (Llera *et al*. 2010). The optimal equivalent damping coefficient of ADAS was 0.329, which was 1.228 times greater than that of the hourglass shape damper. Therefore, ADAS with a greater optimal equivalent damping coefficient than the hourglass shape damper had a considerably better energy dissipation capacity.

3.5.4 Skeleton curve

The ADAS test models' skeleton curves are shown in Fig. 16. They were typically bilinear, with yield occurring at 2.97 and −2.96 mm. We also calculated the percentage difference in the bearing capacity between HNQ-10 and HNQ-5 and that between HNQ-35 and HNQ-5 at each displacement amplitude. For example, L-10 = 100% ×(HNQ-10 -HNQ-5)/HNQ-5; the calculation results are shown in Fig. 17.

(1) The greater the neck width, the greater the damper bearing capacity.

(2) When the damper displacement was less than 3 mm, there was almost no difference in the three models' bearing capacities. When the displacement was increased, the difference in the bearing capacity between HNQ-10 and HNQ-5, and between HNQ-35 and HNQ-5, increased. This is because the DH plates were subjected to bending stresses under small deformations. As the deformations increased, the axial tension in the direction of the DH plate increased. The greater the neck width, the stiffer the damper plates, and the greater the tensile bearing stress in the DH plate. This indicates that, when the neck width is too large, the damper's elastic bearing capacity increases rapidly, which is not conducive to protecting the main structure.

3.5.5 Stiffness degradation

The equivalent secant stiffness k_i is

$$k_i = \frac{\left|F_i^{pull}\right| + \left|F_i^{push}\right|}{\left|\Delta_i^{pull}\right| + \left|\Delta_i^{push}\right|} \tag{26}$$

where F_i^{pull} and F_i^{push} represent the peak tension and peak pressure in the i^{th} hysteretic loading, respectively, and Δ_i^{pull} and Δ_i^{push} represent the peak tension displacement and peak pressure displacement in the i^{th} hysteretic loading, respectively.

The stiffness degradation coefficient β_i is

$$\beta_i = \frac{k_i}{k_0} \tag{27}$$

where i = 1, 2, 3…, k_0 is the equivalent secant stiffness of the damper when the displacement amplitude of the test reached 2 mm (first-order displacement amplitude). The equivalent secant stiffness, and the stiffness degradation coefficient of the ADAS test models, are shown in Fig. 18 and Fig. 19, respectively.

The results show the following. (1) As the neck width increased, the damper's equivalent secant stiffness increased. This is because a relatively large neck width provides additional stiffness to the damper. (2) After the damper entered the elastic-plastic stage, the stiffness degradation coefficient decreased linearly. The damper stiffness quickly reduced to less than 1/2 the original. A relatively small stiffness degradation coefficient helped protect the main structure. The damper stiffness degradation coefficient initially increased, and then decreased, as the neck width increased. When the displacement was 12 mm, the HNQ-10 stiffness degradation coefficient was 27.58% higher than HNQ-5, and the HNQ-35 stiffness degradation coefficient was 7.64% lower than HNQ-10.

3.5.6 DH plate strain for variable amplitude loading

(1) DH plate unilateral strain

The unilateral strain of the DH plate is shown in Fig. 20.

Note that SG-13 in Fig. 20 indicates the strain gauge number 13. With the increased neck width, the consistency of the unilateral strain of the DH plate was initially good and then became poor. The unilateral strains maximum deviations for HNQ-5, HNQ-10, and HNQ-35 were 49%, 28%, and 69%, respectively, indicating the DH plate with a properly defined neck width experiences simultaneous yield energy dissipation.

(2) Neck strain

The neck strain is shown in Fig. 21.

When HNQ-5 yielded, the strains of SG-16 and SG-22 quickly overflowed. It showed that when the neck width was rather small, the neck strain rapidly increased owing to the tensile force along the height of the DH plate, validating the theory that the film effect sharply increases with decreased neck width (Section 2.3). When HNQ-10 yielded, the neck strain began to increase, but it did not overflow; the neck dissipated energy without a significant concentration of strain, thus maintaining the fatigue performance of the damper. There was essentially zero strain reported for the HNQ-35 neck strain gauge, verifying that HNQ-35 did not fracture in the neck during the constant-amplitude loading test. It showed that when the neck width was rather large, the deformation of the neck was very small, and the neck did not contribute to energy dissipation.

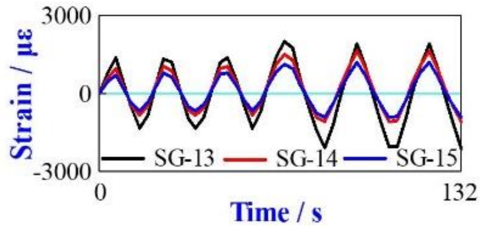

(a) HNQ-5

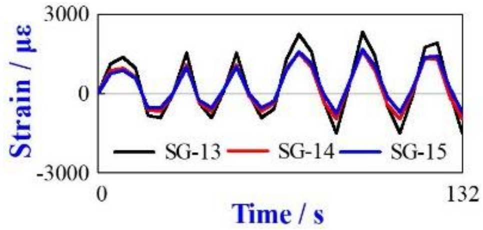

(b) HNQ-10

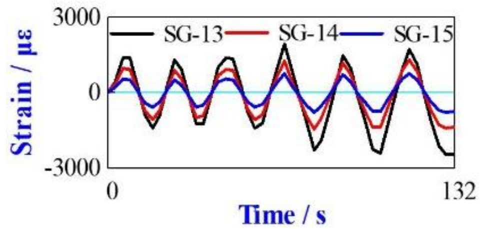

(c) HNQ-35

Fig. 20 DH plate unilateral strain

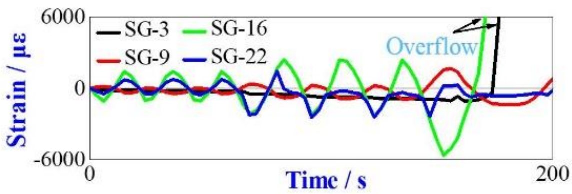

(a) HNQ-5

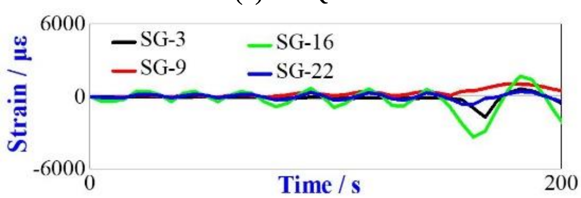

(b) HNQ-10

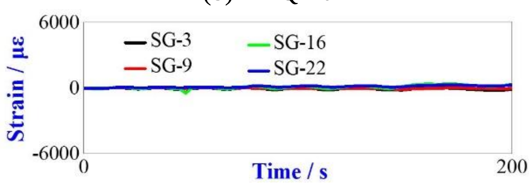

(c) HNQ-35

Fig. 21 Neck strain

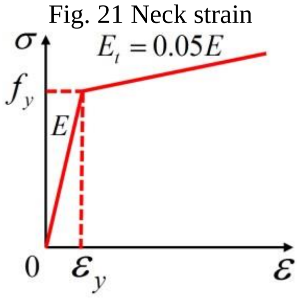

Fig. 22 Constitutive model

4. Finite element analysis

The ADAS was simulated using the finite element software ANSYS. The solid element SOLID186 was selected, considering the nonlinearity and large deformation of the material, and was suitable for generating an irregular mesh model. An isotropic and kinematic hardening material model, taking into account the Bauschinger effect, was applied. The kinematic hardening property simulated the plastic behavior of steel under reciprocating action after the steel yielded. The skeleton curve (Fig. 16) showed a material constitutive that can be approximated by the bilinear model (Hao *et al.* 2018). The specimens' mechanical properties were obtained from the test results. The yield strength was 306.33 MPa, the elastic modulus E was 2.10×10^{5} MPa, the second stiffness coefficient after yield was 0.05, and the tangential modulus E_t was 10500 MPa. The Poisson's ratio v was 0.3. The constitutive model of the DH steel plate is shown in Fig. 22. The ANSYS free mesher was used to create the solid element mesh. The top plate of the damper finite element model was fixed, and the damper's horizontal plates were released in the horizontal constraints. A cyclic vertical displacement was applied to the top plate, and the loading sequence is shown in Fig. 8.

4.1 Results of ANSYS analysis

4.1.1 Von-Mises stress plots

The von-Mises stress plots of the ADAS FEA results are shown in Fig. 23.

When the displacement reached 3 mm, all the HNQ-5 and HNQ-10 DH plates yielded, while near the neck, HNQ-35 remained elastic. At 3 mm, HNQ-5 showed a stress concentration in the neck, which was more apparent under large displacements. At 12 mm, HNQ-10 showed a stress concentration in the neck, while HNQ-35 had a high level of stress near the fillet. When HNQ-35 was under a large displacement load, there was a concentration of stress on the inside of the single limb. As the displacement load increased, the HNQ-5 neck stress increased proportionately more than the other models. The HNQ-35 neck stress increased the least, where part of the neck remained elastic even under large displacements. When the displacement was 24 mm, the stress concentration near the fillet of HNQ-35 was more apparent than that of HNQ-10. The von-Mises stress results were consistent with the test results, indicating that the FEA model can simulate the actual working state of ADAS.

4.1.2 Cumulative equivalent plastic strain

The cumulative equivalent plastic strain (EPEQ) reflects the damper's fatigue performance and its energy dissipation capacity. The EPEQ of ADAS after variable-amplitude loading is shown in Fig. 24.

The EPEQ of HNQ-5 was highly concentrated in the neck. This stress concentration resulted in the damper's poor low cycle fatigue performance, and failure before full energy dissipation occurred. The EPEQ in the neck of HNQ-10 was larger than that in HNQ-5 but was distributed more uniformly. The EPEQ of HNQ-35 was relatively large near the fillet and rather small in the neck.

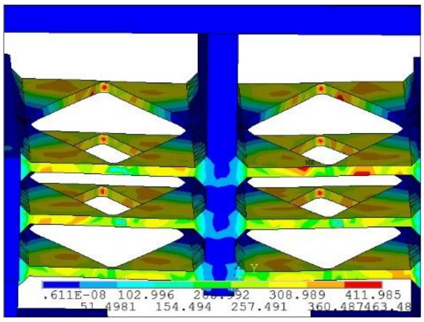

(a) HNQ-5 (displacement 3 mm)

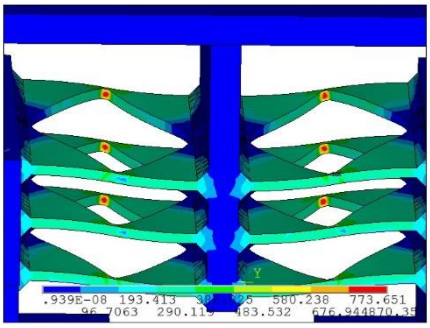

(b) HNQ-5 (displacement 12 mm)

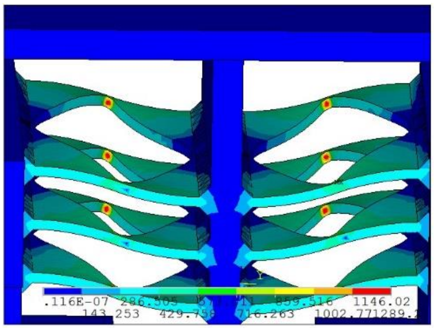

(c) HNQ-5 (displacement 24 mm)

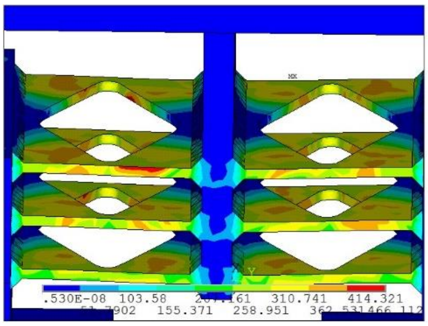

(d) HNQ-10 (displacement 3 mm)

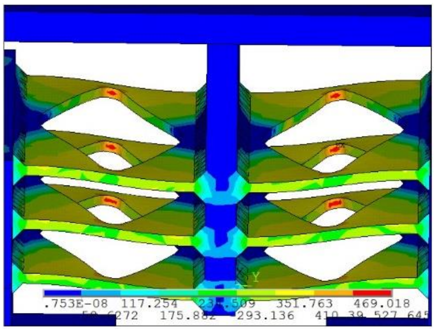

(e) HNQ-10 (displacement 12 mm)

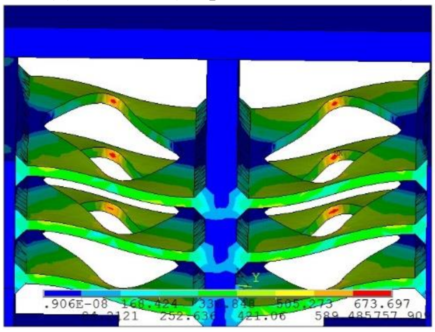

(f) HNQ-10 (displacement 24 mm)

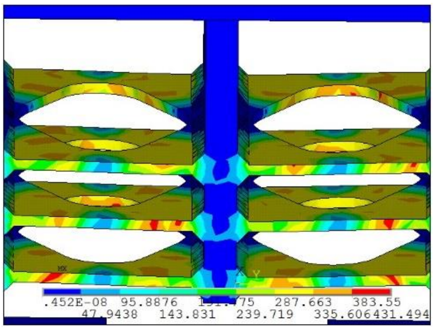

(g) HNQ-35 (displacement 3 mm)

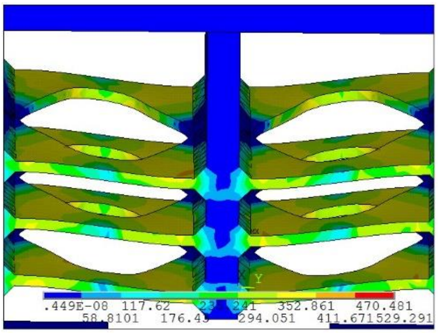

(h) HNQ-35 (displacement 12 mm)

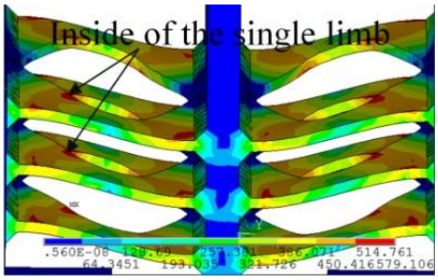

(i) HNQ-35 (displacement 24 mm)

Fig. 23 Von-Mises stress plots

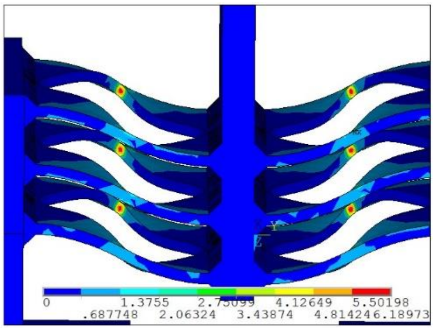

(a) HNQ-5

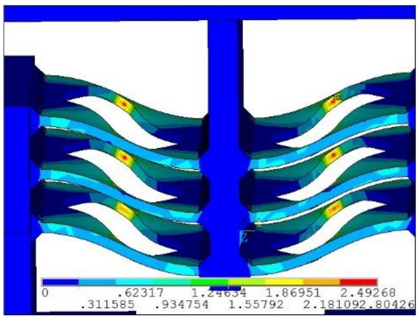

(b) HNQ-10

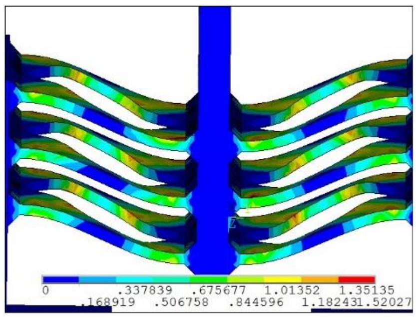

(c) HNQ-35

Fig. 24 Cumulative equivalent plastic strain

Table 1 Comparison of the ADAS performance parameters

Damper / Core performance parameters			HNQ-5	HNQ-10	HNQ-35
Elastic stiffness (kN/mm)	Test value		22.64	25.36	28.95
	FEM value		23.93	28.37	32.78
	Theoretical value		37.59	39.5	49.06
	Error	FEM value	5.70%	11.87%	13.23%
		Theoretical value	66.03%	55.76%	69.46%
Yield load (kN)	Test value		68.21	75.04	85.35
	FEM value		71.31	81.83	92.04
	Theoretical value		75.81	78.42	91.49
	Error	FEM value	4.54%	9.05%	7.84%
		Theoretical value	11.14%	4.50%	7.19%
Yield displacement (mm)	Test value		3.01	2.96	2.94
	FEM value		2.98	2.88	2.81
	Theoretical value		2.02	1.99	1.87
	Error	FEM value	1.00%	2.70%	4.42%
		Theoretical value	32.89%	32.77%	36.39%

The EPEQ variation along the DH plate height is shown in Fig. 25, where the DH plate height (150 mm near the core plate) was plotted along the ordinate, and the maximum EPEQ at a certain height was plotted along the abscissa.

The maximum EPEQ of HNQ-10 was 54.77% lower than that of HNQ-5, indicating that increased neck width reduced stress concentrations and improved the damper's fatigue performance. The EPEQ of HNQ-35 near the core plate (1.52) was twice that of HNQ-35 near the inner plate (0.76), indicating that the welds near the core plate were prone to fatigue. The conclusions obtained from the EPEQ analysis results were consistent with the test results, indicating that the FEA model could be used to simulate the actual working response of the ADAS.

To analyze the relationship between the neck width and the damper's fatigue performance in more detail, the fixed DH plate's geometrical dimensions and displacements were used to establish an ADAS finite element model with eight different neck widths. According to the Coffin-Manson fatigue relationship (Xing and Guo 2003), the strain amplitude could be used to analyze the fatigue performance of ADAS. The variation of the damper strain amplitude is shown in Fig. 26.

When the neck width was small, the film strain caused by the film effect was severe. When the neck width exceeded 16 mm, the strain amplitude increased linearly with the increase in neck width, indicating that the damper's fatigue performance decreased with increased neck width. Therefore, it is necessary to propose a design neck width to alleviate the damper's strain concentration.

4.2 Hysteresis loop

The hysteresis loops of three ADAS tests and FEM are shown in Fig. 27. The FEA results were in good agreement with the test results.

The results of the damper tests, FEA, and theoretical calculations are summarized in Table 1. The error values represent the ratio of the test data and the results of the FEA and theoretical calculations.

As the neck width increased, the elastic stiffness and the yield load increased, and the yield displacement decreased slightly. The error between the FEA value of the performance parameters and the test value was less than 15%, indicating the FEA was satisfactory. The error between the theoretical value of the yield load and the test value was less than 15%, indicating the theoretical equation for the yield load was satisfactory. The error between the theoretical value of the elastic stiffness and the test value was approximately 60%, and the theoretical value was larger than the test value. This may be because of gaps in the test device joints or the stress concentrations in the DH plate. It is recommended that the bolted connections must be secured in engineering applications.

5. Design neck width and elastic stiffness correction

The data verified the FEA model's accuracy. The following section discusses the in-depth FEA of ADAS with more variance in the design parameters.

5.1 Design neck width

The FEA and test results validated the theoretical equation of the minimum neck width (Eq. 23). Because the energy dissipation performance is an important factor in evaluating the damper, the maximum neck width could be determined by the damper's energy dissipation coefficient. Many FEA models with varying design parameters were established to calculate the damper's energy dissipation coefficient. As the neck width increased from the minimum neck width, the energy dissipation coefficient increased and then decreased. The relationship between the energy dissipation coefficient and the neck width is shown in Fig. 28, where H, 280, 220, 8 respectively represents the length, width, and thickness of the DH plate.

When the size of the DH plate was constant, a design neck width can optimize the damper's dissipation coefficient; this neck width was selected as the maximum neck width. α is the ratio of the maximum neck width to the minimum neck width. We assumed that the relation between α and the height H and the thickness t of the DH plate is as follows:

$$\alpha = aH + bt \tag{28}$$

where a and b are the curve fitting parameters.

The curve fitting of α was performed using the 1stOpt data processing software, and the results are shown in Fig. 29. The fitting value was close to the true value, indicating the accuracy of Eq. (28).

Plugging the curve fitting results into Eq. (28):

$$\alpha = 0.0102H - 0.0366t \tag{29}$$

The square of the correlation coefficient of the fitting was 0.9684; thus, the curve fitting result of Eq. (29) was in

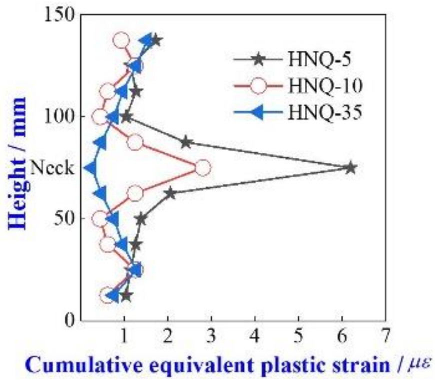

Fig. 25 EPEQ distribution along the height of the DH plate

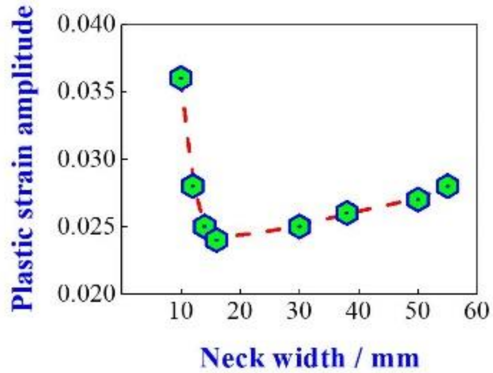

Fig. 26 Variation of the damper strain amplitude

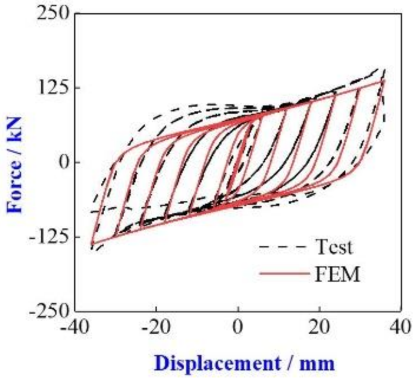

(a) HNQ-5

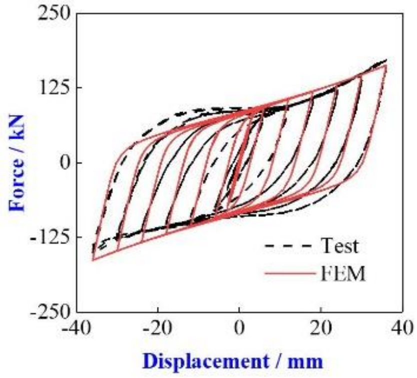

(b) HNQ-10

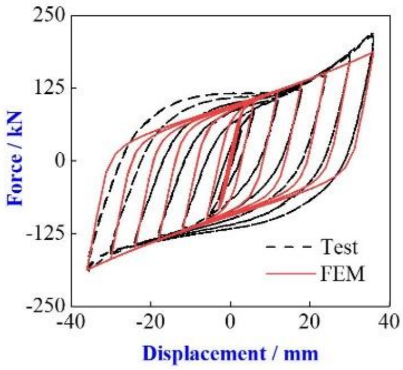

(c) HNQ-35

Fig. 27 Hysteresis loops of the three ADAS

good agreement with the actual value. The maximum neck width B_{max} of the DH plate is

$$B_{max} = \alpha B_{min} \tag{30}$$

The design neck width B_o is

$$B_{min} \le B_o \le \alpha B_{min} \tag{31}$$

Using the test DH plate dimensions of $B = 280mm, H = 150mm, t = 8mm$, the design neck width B_o calculated by Eq. (31) is

$$9.7mm \le B_o \le 12.0mm$$

These results demonstrate that the neck width of HNQ-10 is proper, while the neck widths of HNQ-5 and HNQ-35 are improper. Thus, the accuracy of the design neck width was verified.

5.2 Elastic stiffness correction

Table 1 shows that the elastic stiffness obtained by Eq. (16) has a large error compared to the test value. To accurately obtain the theoretical value of the elastic stiffness of ADAS, a large number of finite element models were used to develop the ADAS modified elastic stiffness equation.

f is the ratio of the theoretical values of the elastic stiffness and the FEM value, that is, the stiffness modified coefficient; the 1stOpt data processing software was used for the fitting of *f*. As shown in Fig. 30, the curve fitting value was close to the actual value.

The curve fitting equation was:

$$\begin{aligned} f &= -0.0012B - 0.0051t + 0.0197\sqrt{H} \\ &+ 0.0070\sqrt{B_1} + 0.7621 \end{aligned} \tag{32}$$

Table 2 Verification of the elastic stiffness correction equation

Damper	Test value / kN / mm	Theoretical value / kN /mm	Correction coefficient	Correction value /kN /mm	Theoretical value error	Corrected value error
HNQ-5	22.64	37.59	0.642	24.13	66.03%	6.58%
HNQ-10	25.36	39.50	0.649	25.64	55.76%	1.10%
HNQ-35	28.95	49.06	0.668	32.77	69.46%	13.20%

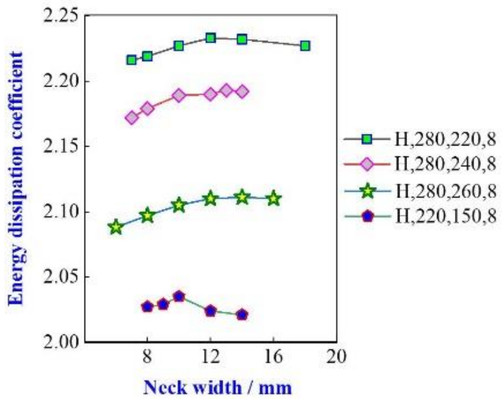

Fig. 28 Relationship between energy dissipation coefficient and neck width

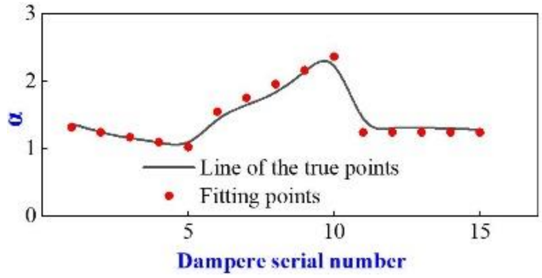

Fig. 29 Fitting results of α

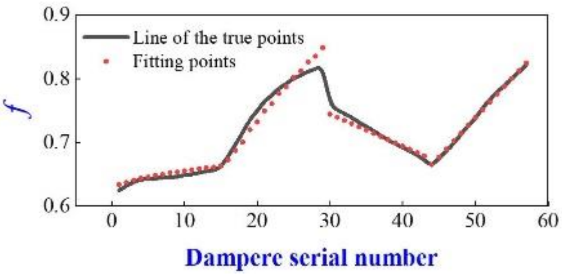

Fig. 30 Fitting results of f

The square of the correlation coefficient of the fitting result was 0.9789, indicating that the modified curve fit of Eq. (32) was in good agreement with the FEA results.

The modified theoretical elastic stiffness K_c of the ADAS is

$$K_c = fK \tag{33}$$

where K is the theoretical value of the damper's elastic stiffness, calculated according to Eq. (18). The theoretical value of the elastic stiffness was obtained by Eq. (18), the elastic stiffness-modified coefficient was obtained by Eq. (32), and the corrected modified elastic stiffness was obtained by Eq. (33). The errors between the theoretical and test values, and the errors between the correction and test values, are shown in Table 2.

Table 2 shows that the mean error between the modified elastic stiffness value, and the test value was 7%. This error was small, especially for HNQ-10, indicating the modified elastic stiffness was close to the test result. Therefore, the elastic stiffness correction equation could be used in the theoretical calculation of the elastic stiffness of ADAS.

6. Conclusions

In this paper, we studied the neck width's influence on ADAS performance. The conclusions are summarized below:

- The ADAS yield load can be easily predicted by analyzing the mechanism. The finite element analysis provided accurate predictions of the elastic stiffness and behavior of the ADAS. As the neck width increased, the elastic stiffness and the yield load increased and the yield displacement slightly decreased.
- An ideal yield state of ADAS can be achieved for the design neck width. The stress concentration was transferred from the fillet to the neck, and the strain concentration was insignificant. Further, cracks appeared in the neck and the fillet, and low cycle fatigue fracture occurred in the neck.
- Reducing the neck width improved the damper's pinch effect, but such reduction may lead to the early damper failure in the event of a large earthquake. As the neck width increased, the damper's dissipation energy significantly increased, but the greater stiffness was not conducive to protecting the main structure because the corresponding neck width was relatively large.
- A design neck width range can be obtained from the mechanical equation of the minimum neck width and the finite element analysis fitting equation of the maximum neck width proposed in this study. The damper with the design neck width can improve fatigue performance while dissipating energy.

Acknowledgements

The research described in this paper was financially supported by the Natural Science Foundation of China (grant nos 51778149).

References

Aghlara, R. and Tahir, M. M. (2018), "A passive metallic damper with replaceable steel bar components for earthquake protection

of structures", *Eng. Struct.*, **159**, 185-197. https://doi.org/10.1016/j.engstruct.2017.12.049.
Basu, D. and Reddy, P. R. M. (2016), "A New Metallic Damper for Seismic Resilience: Analytical Feasibility Study", *Structures*, **7**, 165-183. https://doi.org/10.1016/j.istruc.2016.06.011.
Briones, B. and Llera, J. C. D. L. (2014), "Analysis, design and testing of an hourglass-shaped copper energy dissipation device", *Eng. Struct.*, **79**:309-321. https://doi.org/10.1016/j.engstruct.2014.07.006.
Chan, R. W. K. and Albermani, F. (2008), "Experimental study of steel slit damper for passive energy dissipation", *Eng. Struct.*, **30**(4),1058-1066. https://doi.org/10.1016/j.engstruct.2007.07.005.
Deng, K., Pan, P., Sun, J., Liu, J. and Xue, Y. (2014), "Shape optimization design of steel shear panel dampers", *J. Construct. Steel Res.*, **99**:187-193. https://doi.org/10.1016/j.jcsr.2014.03.001.
Ghabraie, K., Chan, R., Huang, X. and Xie, Y.M. (2010), "Shape optimization of metallic yielding devices for passive mitigation of seismic energy", *Eng. Struct.*, **32**(8), 2258-2267. https://doi.org/10.1016/j.engstruct.2010.03.028.
Hao, L. F, Zhang, R. F, Jin, K. (2018), "Direct design method based on seismic capacity redundancy for structures with metal yielding dampers", *Earthq. Eng. Struct. Dynam.,* **47**(2), 515-534. DOI: https://doi.org/10.1002/eqe.2977.
Hedayat and Ahmad, A. (2015), "Prediction of the force displacement capacity boundary of an unbuckled steel slit damper", *J. Construct. Steel Res.*, **114**:30-50. https://doi.org/10.1016/j.jcsr.2015.07.003.
Ke, K. and Chen, Y. (2014), "Energy-based damage-control design of steel frames with steel slit walls", *Struct. Eng. Mech.*, **52**(6), 1157-1176. http://dx.doi.org/10.12989/sem.2014.52.6.1157.
Lee, C., Ju, Y. K., Min, J., Lho, S. and Kim, S. (2015), "Non-uniform steel strip dampers subjected to cyclic loadings", *Engineering Structures*, **99**:192-204. https://doi.org/10.1016/j.engstruct.2015.04.052.
Lee, C. H., Lho, S. H., Kim, D. H., Oh, J. and Ju, Y. K. (2016), "Hourglass-shaped strip damper subjected to monotonic and cyclic loadings", *Eng. Struct.*, **119**:122-134. https://doi.org/10.1016/j.engs-truct.2016.04.019.
Llera, J. C. D. L., Esguerra, C., José, L., Almazán. (2010), "Earthquake behavior of structures with copper energy dissipators", *Earthq. Eng. Struct. Dynam.*, **33**(3), 329-358. https://doi.org/10.1002/eqe.354.
Mirzaei, M., Akbarshahi, H., Shakeri, M. and Sadighi, M. (2012), "Multidisciplinary optimization of collapsible cylindrical energy absorbers under axial impact load", *Struct. Eng. Mech.*, **44**(3), 325-337. http://dx.doi.org/10.12989/sem.2012.44.3.325.
Nakashima, M. (1995), "Strain-hardening behavior of shear panels made of low-yield steel. I: Test", *J. Struct. Eng.*, **121**(12), 1742-1749. https://doi.org/10.1061/(ASCE)0733-9445(1995)121:12(1742).
Sabouri-Ghomi, S. Payandehjoo, B. (2017), "Analytical and Experimental Studies of the Seismic Performance of Drawer Bracing System (DBS)", *J. Civil Eng.*, **15**(8), 1087-1096. https://doi.org/10.1007/s40999-017-0240-5.
Shih, M. H., Sung, W. P. (2005), "A model for hysteretic behavior of rhombic low yield strength steel added dam-ping and stiffness", *Comput. Struct.*, **83**(12-13), 895-908. https://doi.org/10.1016/j.compstruc.2004.11.012.
Skinner, R. I., Kelly, J. M., Heine, A. J. (2010), "Hysteretic dampers for earthquake-resistant structures", *Earthq. Eng. Struct. Dynam.*, **3**(3), 287-296. https://doi.org/10.1002/eqe.4290030307.
Teruna, D. R., Majid, T. A., Budiono, B. (2015), "Experimental Study of Hysteretic Steel Damper for Energy Dissipation Capacity", *Adv. Civil Eng.*, **2015**, 1-12. http://dx.doi.org/10.1155/2015/631726.
Tsai, K. C., Chen, H. W., Hong, C. P. (1993), "Design of Steel Triangular Plate Energy Absorbers for Seismic-Resistant Construction", *Earthq. Spectra*, **9**(3), 505-528. https://doi.org/10.1193/1.1585727.
Vosooq, A. K. and Zahrai, S. M. (2013), "Study of an innovative two-stage control system: Chevron knee bracing & shear panel in series connection", *Struct. Eng. Mech.*, **47**(6), 881-898. http://dx.doi.org/10.12989/sem.2013.47.6.881.
Wang, A.J. (2017), "Experimental studies into a new type of hybrid outrigger system with metal dampers", *Structural Eng. Mech.*, **64**(2), 183-194. https://doi.org/10.12989/sem.2017.64.2.183.
Whittaker, A. S., Bertero, V. V., Thompson, C. L. and Alonso, L.J. (1991), "Seismic Testing of Steel Plate Energy Dissipation Devices", *Earthq. Spectra*, **7**(4), 563-604. https://doi.org/10.1193/1.1585644.
Xing, S. T. and Guo, X. (2003), "Study on mechanical behavior and effectiveness of a new type of mild steel damper", *Earthq. Eng. Eng. Vib. (Chinese)*, **23**(6), 179-186. https://doi.org/10.3969/j.issn.1000-1301.2003.06.029.
Xu, Y. H., Li, A. Q., Zhou, X. D. and Sun, P. (2010), "Shape Optimization Study of Mild Steel Slit Dampers", *Adv. Mater. Res.*, **168-170**, 2434-2368. https://doi.org/10.4028/www.scientific.net/AMR.168-170.2434.
Zhang, C., Zhou, Y., Weng, D. G., Lu, D.H. and Wu, C.X. (2015), "A methodology for design of metallic dampers in retrofit of earthquake-damaged frame", *Struct. Eng. Mech.*, **56**(4), 569-588. http://dx.doi.org/10.12989/sem.2015.56.4.569.

PL